

ANFIS based Control Strategy for Low Voltage Ride through Capability in DFIG based Wind Farm

B. Sudhakar Naik¹, S. Sunil Naik²

¹Student, Department of Electrical and Electronics Engineering, JNTUA Anantapur, Andhra Pradesh, India

²Lecturer, Department of Electrical and Electronics Engineering, JNTUA Anantapur, Andhra Pradesh, India.

ABSTRACT

This paper deals with the operation of doubly fed induction generator (DFIG) with Adaptive Neuro Fuzzy interface system (ANFIS) using rotor-side converter (RSC). Protection against voltage dips is very important for a transient stability in doubly fed induction generator (DFIG). Conventional crowbar circuits have been used for protection of DFIGs; however, they may be insufficient in some transient situations. Therefore, the Low Voltage Ride through (LVRT) capability was enhanced by a Demagnetization Current Controller (DCC) for the purpose of transient analysis. The main contribution of this work lies in the control of RSC using Adaptive Neuro Fuzzy interface system (ANFIS). In addition, both stator and rotor circuit electromotive forces were modeled in a DFIG. The performances of the DFIG models with DCC, without DCC and with ANFIS were compared. Modeling was carried out in a MATLAB/SIMULINK environment. A comparison of system behaviors was made between three phase faults with and without a stator rotor dynamic. Parameters for the DFIG including output voltage, speed, electrical torque variations and d-q axis rotor-stator current variations in addition to a 34.5 kV bus voltage were examined. It was found that in the DFIG model the system became stable in a short time when using an ANFIS.

Keywords : Doubly Fed Induction Generator (DFIG), Demagnetization Current Controller (DCC), Adaptive Neuro Fuzzy Interface System (ANFIS), LVRT.

I. INTRODUCTION

With the increase in population and industrialization, the energy demand has increased significantly. However, the conventional energy sources such as coal, oil, and gas are limited in nature. Now, there is a need for renewable energy sources for the future energy demand [1]. The other main advantages of this renewable source are eco-friendliness and unlimited in nature [2]. Due to technical advancements, the cost of the wind power produced is comparable to that of conventional power plants. Therefore, the wind energy is the most preferred out of all renewable energy sources [3]. In the initial days, wind turbines have been used as fixed speed wind turbines with squirrel cage induction generator and capacitor banks. Most of the wind turbines are fixed speed because of their simplicity and low cost [4]. By observing wind turbine characteristics, one can clearly identify that for extracting maximum power, the machine should run at varying rotor speeds at different wind speeds. Using modern power electronic converters, the machine is able to run at adjustable speeds [5].

Therefore, these variable speed wind turbines are able to improve the wind energy production [6]. Out of all variable speed wind turbines, doubly fed induction generators (DFIGs) are preferred because of their low cost [7]. The other advantages of this DFIG are the higher energy output, lower converter rating, and better utilization of generators [8]. These DFIGs also provide good damping performance for the weak grid [9]. Independent control of active and reactive power is achieved by the decoupled vector control algorithm presented in [10] and [11]. This vector control of such system is usually realized in synchronously rotating reference frame oriented in either voltage axis or flux axis. In this work, the control of rotor-side converter (RSC) is implemented in voltage-oriented reference frame. Grid code requirements for the grid connection and operation of wind farms are discussed in [12]. Response of DFIG-based.

Another control technique in the DFIG uses a series voltage source for the regulation of the transient instability state in the rotor-side converter circuit, and a

comparison was made by combining the series voltage source control with a conventional crowbar unit in the DFIG [17]. In a DFIG-based wind farm, the LVRT capability was enhanced with a linear quadratic feedback centralized control unit in the rotor- and grid-side converters. This centralized control was effective for various fault types in the DFIG [12]. The proposed LVRT control strategy provides new flux tracking for a short circuit state in the DFIG. In the proposed control strategy, in addition to rotor electromotive force modeling during faults, the stator flux linkage is provided by a rotor-side converter control [14, 15]. In Refs. [16, 17], the behavior of the DFIG including the generator machine magnetizing current control, was analyzed during voltage dips using models in the dominant frequency. The aim was to enhance the system response during balanced and unbalanced voltage dips in the DFIG. Power Oscillation Damping (POD) is important for regulates voltage sags-swells in besides the overcurrent sin the DFIG based wind farm in grid faults, and therefore, significantly enhances the LVRT capability of the DFIG based wind farm[21–22]. In this study, dynamic modeling with a base voltage source was developed for the LVRT capability of both stator and rotor circuits in a DFIG. Additionally, for transient stability conditions, the LVRT was enhanced by a DCC. A comparison was drawn between the systems developed through stator- and rotor-based electromotive forces with and without the DCC during various faults. Modeling of wind farm.

II. Modeling of Wind Farm

The DFIG of a wind turbine is basically a wound rotor induction machine with the stator windings directly connected to the three phase grid and with the rotor windings connected to a back-to back converter, consisting of a grid-side converter and a rotor side converter connected to a common DC bus. The behavior of the DFIG is governed by these converters and their controllers in both steady-state and transient conditions. The converters control the rotor voltage in magnitude and phase angle and therefore, they are used for active and reactive power control [18, 19]. The equivalent circuit of the induction generator, seen from the stator and rotor side, can be seen in Fig. 1. The rotor model expresses the mechanical power extracted from the wind

as a function of the wind speed, the blade tip speed ratio and the blade pitch angle, as defined in

$$P_w = \frac{1}{2} \rho A u^3 C_p(\lambda, \theta) \quad (1)$$

Where P_w is the mechanical power extracted by the wind turbine rotor, ρ is the air density, A is the area of the rotor disk, u is the wind

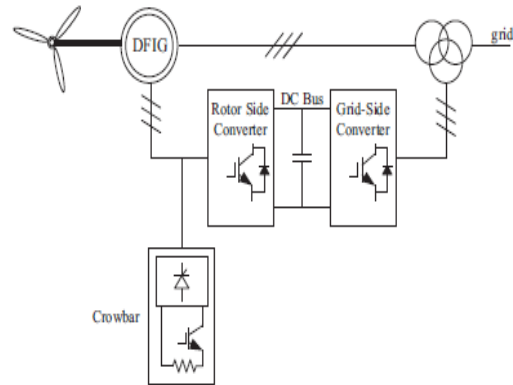


Fig. 1. DFIG circuit modeling.

Speed and C_p is the power coefficient. The power coefficient terms the rotor aerodynamics as a function of both tip speed ratio k and the pitch angle of the rotor blades h . The tip speed ratio is described as the ratio between the blade tip speed and the wind speed, explained as:

$$\lambda = \frac{w_r R}{u} \quad (2)$$

Where w_r is the rotor speed and R is the radius of the wind turbine rotor. The power extracted from the wind is maximized when the rotor speed is such that the power coefficient is at maximum, which occurs for a determined tip speed ratio. The control system of the DFIG wind turbine assures that the variable speed operation maximizes the output power for a wide range of wind speeds, according to the optimum power extraction curve, given as:

$$P_{op} = K_{op} w_r^2 \quad (3)$$

As the wind turbine limits the output power to the rated power of the generator for high winds, the power–speed curve is the rated power. This power–speed curve gives a dynamic reference for the control system of the DFIG wind turbine [21]. The drive train of the DFIG wind turbine has been defined in two mass models:

$$T_w - T_m = 2H \frac{dw_r}{dt} \quad (4)$$

$$T_m = D_m(w_r - w) + K_m \int (w_r - w) dt \quad (5)$$

where T_w is the mechanical torque from the wind turbine rotor shaft, T_m is the mechanical torque from the generator shaft, H is the rotor inertia, and K_m and D_m

are the stiffness and damping of the mechanical coupling [21]. The purpose of the rotor-side converter controller is to control the DFIG output active power for tracking the input of the wind farm torque, and to maintain the terminal voltage to control setting. The active power and voltage are controlled independently by V_{dr} and V_{qr} , respectively. The control equations are given as:

$$\frac{dx_1}{dt} = P_{ref} + P_s \quad (6)$$

$$I_{qr_ref} = K_{p1}(P_{ref} + P_s) + K_{i1}x_1 \quad (7)$$

$$\frac{dx_2}{dt} = I_{qr_ref} - I_{qr} = K_{p1}(P_{ref} + P_s) + K_{i1}x_1 - I_{qr} \quad (8)$$

$$\frac{dx_3}{dt} = v_{s_ref} - v_s \quad (9)$$

$$I_{dr_ref} = K_{p3}(v_{s_ref} - v_s) + K_{i3}x_3 \quad (10)$$

$$\frac{dx_4}{dt} = I_{qr_ref} - I_{qr} = K_{p3}(v_{s_ref} - v_s) + K_{i3}x_3 - I_{qr} \quad (11)$$

$$v_{qr} = K_{p2}(K_{p1}\Delta P + K_{i1}x_1 - I_{qr}) + K_{i2}x_2 + sw_s L_m I_{ds} + sw_s L_{rr} I_{qr} \quad (12)$$

$$v_{dr} = K_{p2}(K_{p3}\Delta v + K_{i3}x_3 - I_{dr}) + K_{i2}x_4 - sw_s L_m I_{qs} - sw_s L_{rr} I_{dr} \quad (13)$$

where K_{p1} and K_{i1} are the proportional and integrating gains of the power regulator, respectively; K_{p2} and K_{i2} are the proportional and integrating gains of the rotor-side converter current regulator, respectively; K_{p3} and K_{i3} are the proportional and integrating gains of the grid voltage regulator, respectively; I_{dr_ref} and I_{qr_ref} are the current control references for the d and q axis components of the generator side converter, respectively; V_{s_ref} is the specified terminal voltage reference; and P_{ref} is the active power control reference. The grid-side converter controller aims to maintain the DC link voltage and control the terminal reactive power. The voltage of the DC link is controlled by I_{dg} while the reactive power is controlled by I_{qg} . The following equations are based on introduction of the intermediate variables $\times 5$, $\times 6$ and $\times 7$:

$$\frac{dx_5}{dt} = v_{dc_ref} - v_{dc} \quad (14)$$

$$I_{dgrid_ref} = -K_{pgrid}\Delta v_{dc} + K_{idgrid}x_5 \quad (15)$$

$$\frac{dx_6}{dt} = I_{dgrid_ref} - I_{dgrid} = -K_{pgrid}\Delta v_{dc} + K_{idgrid}x_5 - I_{dgrid} \quad (16)$$

$$\frac{dx_7}{dt} = I_{qgrid_ref} - I_{qgrid} \quad (17)$$

$$\Delta v_{dgrid} = K_{pgrid} \frac{dx_6}{dt} + K_{idgrid}x_6 = K_{pgrid}(-K_{pdgrid}\Delta v_{dc} + K_{idgrid}x_5 - I_{dgrid}) + K_{idgrid}x_6 \quad (18)$$

$$\Delta v_{qgrid} = K_{pgrid} \frac{dx_7}{dt} + K_{idgrid}x_7 = K_{pgrid}(I_{qgrid_ref} - I_{qgrid}) + K_{idgrid}x_7 \quad (19)$$

Where K_{pgrid} and K_{idgrid} are the proportional and integrating gains of the DC bus voltage regulator, respectively. K_{pgrid} and K_{idgrid} are the proportional and integrating gains of the grid-side converter current regulator, respectively; is the voltage control reference of the DC link; v_{dc_ref} and I_{qgrid_ref} is the control reference for the q axis component of the grid-side converter current [21]. The DFIG exploits active and reactive powers from the rotor current and grid voltage. The calculations of the active and

$$P_s = v_{grid} \frac{L_m}{L_s} I_{dqr} \quad (20)$$

$$Q_s = v_{grid} \frac{L_m}{L_s} I_{dqr} - \frac{v_{grid}^2}{w_s L_s} \quad (21)$$

The full order DFIG model is represented by five equations, considering the generator's variables in the d-q synchronous reference frame. The equations for the stator and rotor windings with the torque equations can be seen as Equations (22), (26);

$$v_{ds} = R_s i_{ds} + w_s \lambda_{qs} + \frac{d}{dt} \lambda_{ds} \quad (22)$$

$$v_{qs} = R_s i_{qs} - w_s \lambda_{ds} + \frac{d}{dt} \lambda_{qs} \quad (23)$$

$$v_{dr} = R_r i_{dr} - sw_s \lambda_{qr} + \frac{d}{dt} \lambda_{dr} \quad (24)$$

$$v_{qr} = R_r i_{qr} + sw_s \lambda_{dr} + \frac{d}{dt} \lambda_{qr} \quad (25)$$

$$M = \lambda_{ds} i_{qs} - \lambda_{qs} i_{ds} \quad (26)$$

The flux-inductance equations can be expressed in d-q coordinates as follows:

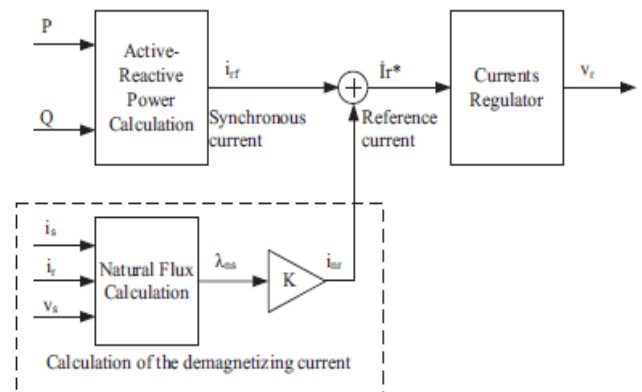


Fig. 2. Reference current control with DCC.

$$\lambda_{ds} = (L_s + L_m)i_{ds} + L_m i_{dr} \quad (27)$$

$$\lambda_{qs} = (L_s + L_m)i_{qs} + L_m i_{qr} \quad (28)$$

$$\lambda_{dr} = (L_r + L_m)i_{dr} + L_m i_{ds} \quad (29)$$

$$\lambda_{dr} = (L_r + L_m)i_{qr} + L_m i_{qs} \quad (30)$$

Reduced order DFIG models were employed to ease computation for the transient analyses. In this model, the stator is represented by a transient voltage source behind a transient reactance where the stator flux derivation is disregarded. The main idea is that the dc components omitted from the stator transient current [18, 21].

$$v_{ds} = R_s i_{ds} - X' i_{qs} + e_{ds} \quad (31)$$

$$v_{qs} = R_s i_{qs} + X' i_{ds} - e_{ds} \quad (32)$$

$$\frac{de_{ds}}{dt} = -\frac{1}{T_o} [e_{ds} - (X - X') \times I_{qs}] + s \times w_s \times e_{qs} -$$

$$w_s \times \frac{L_m}{L_m + L_s} \times v_{dr}$$

$$(33)$$

$$\frac{de_{qs}}{dt} = -\frac{1}{T_o} [e_{qs} + (X - X') \times I_{qs}] - s \times w_s \times e_{qs} -$$

$$w_s \times \frac{L_m}{L_m + L_s} \times v_{qr}$$

$$(34)$$

$$v_{dr} = R_r i_{dr} + s w_s \lambda_{qr} + \frac{d}{dt} \lambda_{dr} \quad (35)$$

$$v_{qr} = R_r i_{qr} - s w_s \lambda_{dr} + \frac{d}{dt} \lambda_{qr} \quad (36)$$

$$M = e_{ds} i_{qs} + e_{qs} i_{ds} \quad (37)$$

In these equations: v_{ds} , v_{qs} , v_{dr} , v_{qr} are the d and q axis voltages of the stator and rotor; i_{ds} , i_{qs} , i_{dr} , i_{qr} are the d and q axis currents of the stator and rotor; K_{ds} , K_{qs} , k_{dr} , k_{qr} are the d and q axis magnetic fluxes of the stator and rotor; E_{ds} and E_{qs} are the d axis and q axis source voltages of the stator; w_s is the angular speed of the stator; s is the slip; R_s and R_r are the stator and rotor resistance; X is the stator reactance; X' is the transient reactance; L_s and L_r are the stator and rotor inductance; L_m is the magnetic inductance; and M is the torque. While the transient open circuit time constant is given in Eq. (39) [21, 22].

$$X' = w_s (L_m + L_s) - \frac{L_m^2}{L_m + L_s} \quad (38)$$

$$T_o = \frac{L_r + L_m}{R_r} \quad (39)$$

The rotor voltage drops as a result of shifts in the steady state operation. However, during transient conditions, in order to reach saturation of the converter, an excessive increase in voltage occurs. As a result, this leads to a loss of rotor current control. Rotor voltage and rotor flux variations are given in Equations (40) and (41);

$$\lambda_{dr} = \frac{L_m}{L_s} \lambda_{ds} + \sigma L_r i_{dr} \quad (40)$$

$$\lambda_{qr} = \frac{L_m}{L_s} \lambda_{qs} - \sigma L_r i_{qr} \quad (41)$$

Here, σ is the rotor damping coefficient. The rotor damping coefficients given in Eq. (42).

$$\sigma = 1 - \frac{L_m^2}{(L_s L_r)} \quad (42)$$

By adding flux Equations (40) and (41) to the voltage equation of rotors. (35) and (36), the following expressions are obtained

$$v_{dr} = \frac{L_m}{L_s} + R_r i_{dr} + \sigma \frac{d}{dt} L_r i_{dr} \quad (43)$$

$$v_{qr} = \frac{L_m}{L_s} + R_r i_{qr} - \sigma \frac{d}{dt} L_r i_{qr} \quad (44)$$

Equations (43) and (44) are divided into two parts. The first part is identified as the electromotive force and zero is used as the open circuit constant. The second part is considered to be only the rotor current. This part causes a voltage dip in rotor resistance and rotor transient inductance.

III. Behavior under voltage dip of DFIG

During normal operation, the stator and rotor d-q fluxes rotate with synchronous speed. With regard to the rotor windings, the flux rotates at slip and synchronous speed. As a result of the electromotive force, a voltage proportional to the slip and synchronous speed can be described by:

$$e_{dqr} = \frac{L_m}{L_s} \lambda_{dqs} w_s S \cong v_{dqs} S \quad (45)$$

This situation changes dramatically in the case of a voltage dip, as has been analyzed in this paper. For example, when the time is zero ($t = 0$), the voltage dip causes the stator to be short circuited. In Equations (40) and (41), ignoring the small voltage dip in the stator resistance, the derivative of the stator flux will be zero. Thus, the flux will remain constant and stop rotating. As the stator flux is fixed to the stator, it is akin to speed with regard to the rotor windings and the speed of the rotor. Accordingly, the electromotive force is given in Eq. (46).

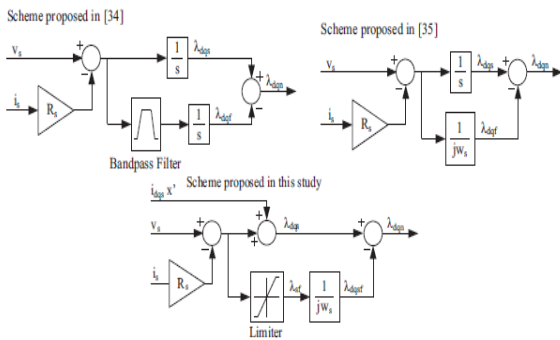
$$e_{dqr}(t = 0) = \frac{L_m}{L_s} \lambda_{dqs} w = \frac{L_m}{L_s} \lambda_{dqs} w_s (1 - S) \cong v_{dqs} (1 - S) \quad (46)$$

In Eq. (46), the slip is indicated by $(1 - S)$ to calculate the transient state of the electromotive force. However, in the normal, steady state, the slip is shown as S .

Generally, partial voltage dips in the stator voltage happen during grid faults. This voltage decrease occurs above zero p u. A partial voltage drop, depending on stator voltage under normal operating conditions, is calculated as seen in Eq. (47).

$$v_{s1} = \left\{ \begin{array}{l} V e^{j\omega_s t} \\ (1-P)V e^{j\omega_s t} \end{array} \right\} \quad (47)$$

Fig. 3. Calculate natural flux in different control



methods.

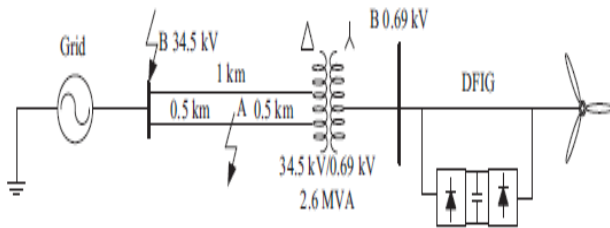


Fig. 4. Test system.

Where v_{s1} is the stator d-q axis partial voltage; V is the crowbar voltage; and p is the voltage dip ratio. While using $t < 0$ for the partial voltage dip in the first part of the equation, during the second part, $t \geq 0.2$ must be used for partial voltage. In the second part of Eq. (47), in addition to using the stator d-q axis, the natural d-q axis flux is used. The calculation for the natural flux is given in Eq. (48).

$$\lambda_{nf}(t = 0) = \frac{pV}{j\omega_s} \quad (48)$$

The new stator d-q axis flux depending on the natural flux is given in Eq. (49).

$$\lambda_{nf}(t) = \frac{(1-P)V}{j\omega_s} e^{j\omega_s t} + \lambda_{nf} \quad (49)$$

During steady state operation, natural flux is called force flux. If the force flux is used during the transient state, there will be a difference in the calculation of the fluxes. This situation would disrupt the synchronism of the angular speed. For this reason, the natural flux is used in

the transient state. However, when the natural flux is used in the transient state, oscillations occur. In order to remove these oscillations, electromotive force is used in the d-q axis [22]. Preliminary values for electromotive force are given in Eq. (50).

$$e_r(t = 0) = \frac{L_m}{L_s} (V(1-P)S - Vp(1-S)) \quad (50)$$

In Eq. (14), the induced rotor voltage consists of two parts. The first part is calculated depending on the slip rate. In this part a small voltage dip may be disregarded. In addition, it is independent from the maximum loading state. In the second part, the $1 - S$ value is associated with the highest voltage dip. In order to compensate for the voltage dip, the induced rotor voltage is supplied by the natural flux. Therefore, the saturated converter is protected and overvoltage in the dc is prevented.

The crowbar unit was developed as the beginning of the search for technical alternatives to protect against disconnecting the rotor-side converter. As seen in the crowbar unit, the difficulty of keeping the converter connected brings about the overvoltage induced by the natural flux in the rotor during a voltage dip [22] aimed to control the current opposite to the natural flux in order to weaken its effect on the rotor. This current is a demagnetizing current. The injection of a current opposite to the magnetic flux in order to reduce the voltage is a known technique used in various applications. The difference with the control aim here is that currently, the technique is solely applied to natural flux. With this method, overvoltage is prevented. In order to minimize the natural flux, natural current is required. The calculation for natural current is given in Eq. (51).

$$i_{nr} = -\frac{L_m}{L_s} \frac{1}{\sigma L_r} \lambda_{nf} \quad (51)$$

With this equation, a form of current against natural flux is provided. Furthermore, in order to reduce rotor voltage, the effect of the transient state of the natural flux is delayed. Both a vector controller and a reference current controller are used to control this natural flux. The reference current controller using DCC is given in Fig.2. The reference current controller is calculated depending on the values of the synchronous current controller and the DCC. The rotor current and rotor voltage values are calculated from the current regulator circuit. The natural flux control units from Ref. [21], Ref. [22] and this paper are given in Fig. 3. For the natural current control, the operation is performed by using the derivative from the stator flux. A band pass filter and

derivative transactions are used for calculating the power flux Ref. [21]. Ref. [22] resembles Ref. [22] in terms of stator flux derivation. However, the natural flux benefits from the synchronous speed. In this paper, owing to the induction generator-based reduced order model, the stator flux derivation was disregarded. Furthermore, in the calculation of the power flux, a limiter and synchronous speed were used.

IV. Design of ANFIS based Controller

Adaptive Neuro Fuzzy Inference system (ANFIS) integrates the best features of fuzzy systems and neural networks, and it has potential to capture the benefits of both in a single frame work. ANFIS is a kind of artificial neural network that is based on Takagi-sugeno fuzzy inference system, which is having one input as done output. Using a given data set, the toolbox function of ANFIS constructs a fuzzy inference system (FIS) whereas the membership function parameters are tuned (adjusted) using a back propagation algorithm. In order to have an idea of optimized ANFIS architecture for proposed control, an initial data is generated from normal PI regulator and the data is saved in workspace of MATLAB. Then the ANFIS command window is opened by typing ANFIS editor in the main MATLAB window. Then the data previously saved in workspace is loaded in the ANFIS command window to generate an optimized ANFIS architecture as shown in Fig.5.

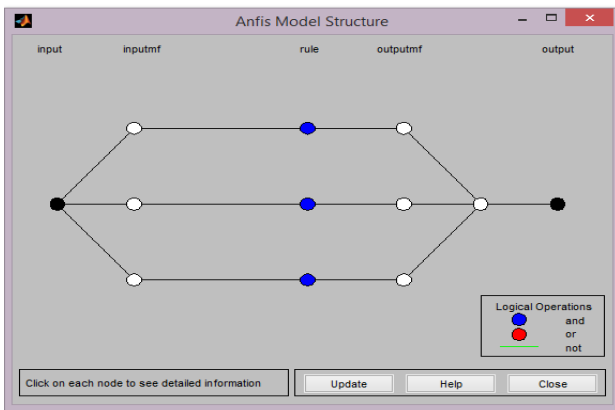


Fig. 5 Optimized ANFIS architecture

In Fig.5 shows schematic of the proposed ANFIS based control architecture. The node functions of each layer in the ANFIS architecture are described as follows:

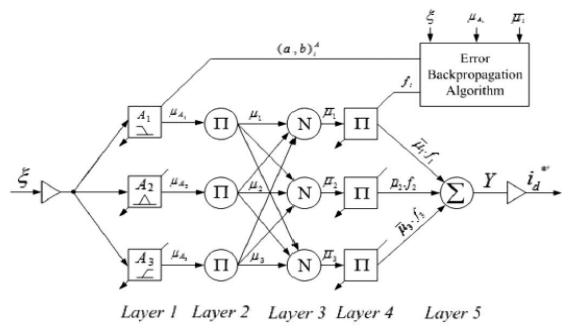


Fig. 5(a) Schematic of the proposed ANFIS-based control architecture.

The error between reference dc-link voltage and actual dc-link voltage ($\xi = V_{dc}^* - V_{dc}$) is given to the neuro-fuzzy controller and the same error is used to tune the precondition and consequent parameters [10]. The control of dc-link voltage gives the active power current component (i_d^*), which is further modified to take in account of active current component injected from RES (I_{Ren}). The node functions of each layer in ANFIS architecture are as described below.

Layer 1: This layer is also known as Fuzzification layer where each node is represented by square. Here, three membership functions are assigned to each input. The trapezoidal and triangular membership functions are used to reduce the computation burden as shown in Fig. 6. And the corresponding node equations are as given below:

$$\mu_{A1}(\varepsilon) = \begin{cases} 1 & \varepsilon \leq b_1 \\ \frac{\varepsilon - a_1}{b_1 - a_1} & b_1 < \varepsilon < a_1 \\ 0 & \varepsilon \geq a_1 \end{cases} \quad (52)$$

$$\mu_{A2}(\varepsilon) = \begin{cases} 1 - \frac{\varepsilon - a_1}{0.5b_2} & |\varepsilon - a_2| \leq 0.5b_2 \\ 0 & |\varepsilon - a_2| \geq 0.5b_2 \end{cases} \quad (53)$$

$$\mu_{A3}(\varepsilon) = \begin{cases} 0 & \varepsilon \leq a_3 \\ \frac{\varepsilon - a_1}{b_1 - a_1} & a_3 < \varepsilon < b_3 \\ 1 & \varepsilon \geq b_3 \end{cases} \quad (54)$$

Where the value of parameters (a_1, b_1) changes with the change in error and accordingly generates the linguistic value of each membership function. Parameters in this layer are referred as premise parameters or precondition parameters.

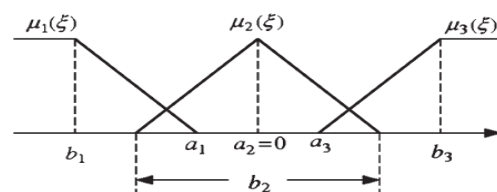


Fig. 6 Fuzzy membership functions.

Layer 2: Every node in this layer is a circle labelled as Π which multiplies the incoming signals and forwards it to next layer

$\mu_i = \mu_{Ai}(\varepsilon_1) \cdot \mu_{Bi}(\varepsilon_2) \dots \dots \dots, i = 1, 2, 3, \dots \dots$. But in our case there is only one input, so this layer can be ignored and the output of first layer will directly pass to the third layer. Here, the output of each node represents the firing strength of a rule.

Layer 3: Every node in this layer is represented as circle. This layer calculates the normalized firing strength of each rule as given below:

$$\bar{\mu}_i = \frac{\mu_i}{\mu_1 + \mu_2 + \mu_3} \quad (54)$$

Layer 4: Every node in this layer is a node function

$$O_i = \bar{\mu}_i \cdot f_i = \bar{\mu}_i (a_0^i + a_1^i \varepsilon) \quad i=1,2,3, \dots \dots$$

Where the parameters (a_0^i, a_1^i) are tuned as the function of input (ζ) . The parameters in this layer are also referred as consequent parameters.

Layer 5: This layer is also called output layer which computes the output as given below: The output from this layer is multiplied with the normalizing factor to obtain the active power current component.

V. Simulation Results

The 0.85MW wind power system shown in Fig. 4 was used to study the transient behavior of the wind turbine grid interaction. The wind turbine generator was represented by two models: the reduced order DFIG model and the enhanced DFIG model within active LVRT, as explained in the previous section. The wind power plant was connected to a 34.5 kV system through a 2.6 MW, 0.69 kV Y/34.5 kV D transformers. There was a distance of 1 km between the plant and the 34.5 kV grid. A 0.69 kV Y/34.5 kV D transformer provided the transmission grid connection. The wind speed was considered to be a constant 8 m/s. The saturation of the transformers was not considered. The 34.5 kV grid-side short circuit power was chosen as 2500 MVA, while the X/R rate was chosen as 7. In the DFIG, a stator resistance of 0.00706 X, rotor resistance of 0.005 X, stator inductance of 0.171 H, rotor inductance of 0.156 H and inertia constant of 3.5 s were selected as the generator parameters.

The impact of the DCC on the system parameters was examined against two transient events. A 3-phase fault was considered as the first transient event. The fault was created in the middle of the transmission line

in the time interval between 0.55 and 0.6 s. The 34.5 kV bus voltage, variations in DFIG output voltage, DFIG angular speed, DFIG electrical torque, and DFIG d-q axis rotor-stator current were observed for the DFIG with and without the DCC.

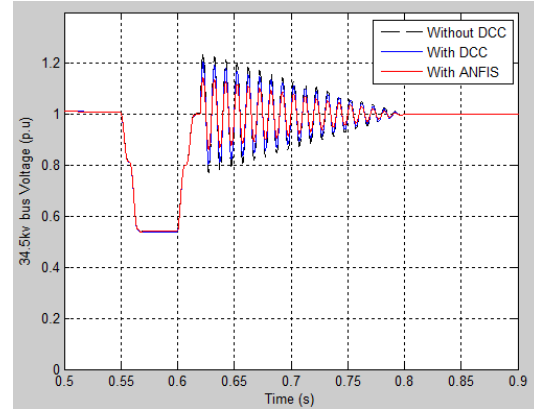


Fig. 7(a) 34.5 kV bus voltage (3 phase fault in bus)

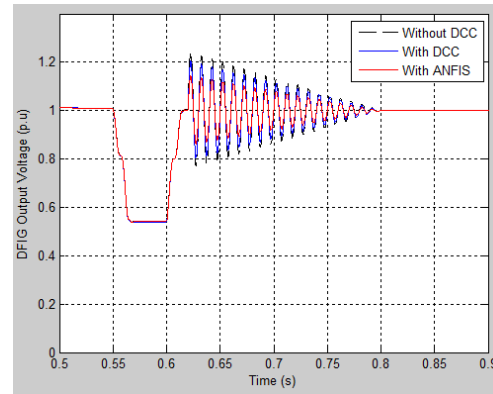


Fig. 7(b) DFIG output voltage (3 phase fault in bus)

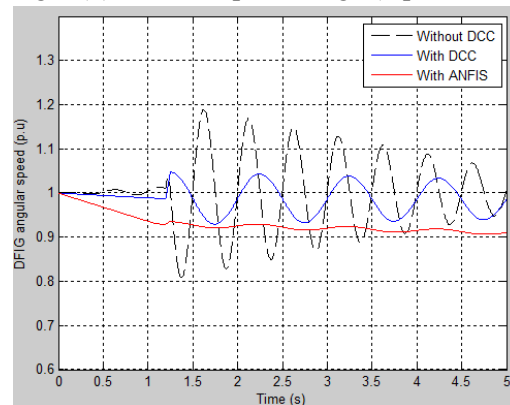


Fig. 7(c) DFIG angular speed (3 phase fault in bus),

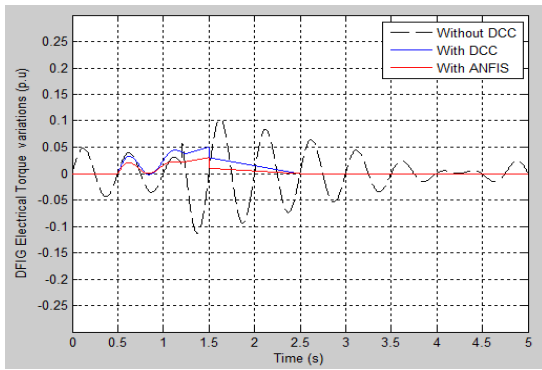


Fig. 7(d) DFIG electrical torque (3phase fault in bus),

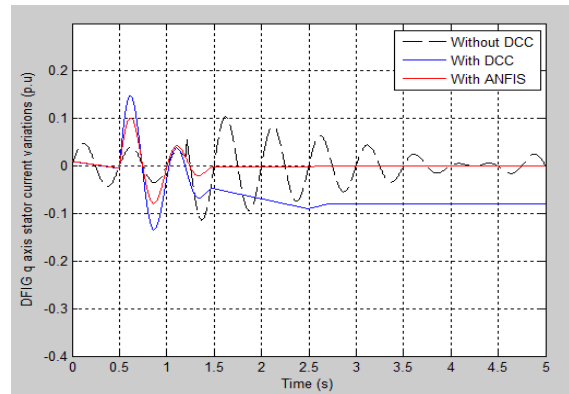


Fig. 7(h) DFIG q axis stator current variations (3 phase fault in bus),

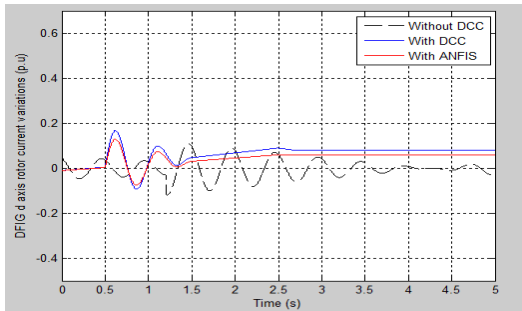


Fig. 7(e) DFIG d axis rotor current variations (3 phase fault in bus),

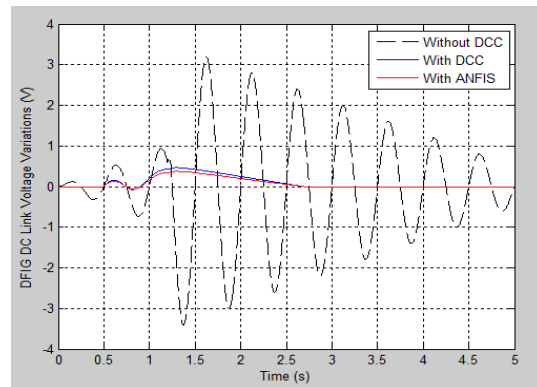


Fig. 7(i) DFIG DC link voltage variations (3 phase fault in bus)

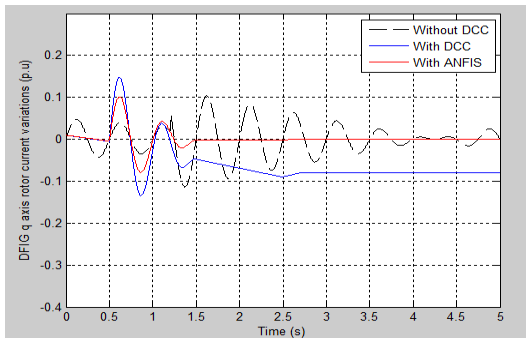


Fig. 7(f) DFIG q axis rotor current variations (3 phase fault in bus),

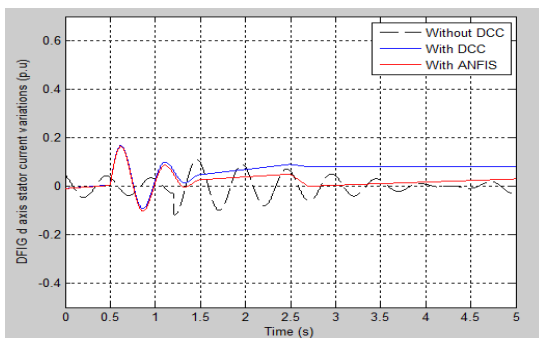


Fig. 7(g) DFIG d axis stator current variations (3 phase fault in bus),

In the 3-phase fault event in the bus B 34.5 kV, the voltage values of 34.5 kV bus and DFIG output were around 0 p.u. without the ANFIS in the DFIG. However, the values increased to 0.2 p.u. with the use of an ANFIS in the DFIG. As happened in the case of the first 3-phase fault, the DCC usage also helped in damping oscillations occurring at the time in several parameters such as the DFIG angular speed, electrical torque, and d-q axis stator current variations. While DFIG angular speed, electrical torque and d-q axes stator and rotor currents with ANFIS was stabilized in nearly 1.25 s, 2.9 s, 2.9 s, 2.9 s after 3 phase fault in middle transmission line, respectively. DFIG angular speed, electrical torque and d-q axes stator currents without ANFIS was stabilized in nearly 0.15 s, 5 s, 6.5 s, 6.5 s after 3 phase fault in middle transmission line, respectively. DFIG DC link voltage variations were observed with and without the DCC in the DFIG model, and the comparisons are shown in Figs. 7 and 8. While DFIG DC link voltage variation with DCC was stabilized in nearly 2.9 s after 3 phase fault in middle transmission line, DFIG DC link voltage variation without DCC was stabilized in nearly

6.5 s after 3 phase fault in middle transmission line. While DFIG DC link voltage variation with DCC was stabilized in nearly 2.9 s after 3 phase fault in 34.5 kV bus, DFIG DC link voltage variation without ANFIS was stabilized in nearly 6.5 s after 3 phase fault in 34.5 kV bus.

VI. Conclusions

This study represents the implementation of an ANFIS for a grid integrated, DFIG based wind farm. A reduced order model was used for the DFIG to ease computation. The transient behaviors of the system with DCC, without DCC and ANFIS were compared in terms of voltage dips. In addition to an ANFIS, the reference current control in the DFIG was enhanced. As a result of an ANFIS and reference current control, the transient stability in the DFIG was enhanced. While oscillation increased considerably in the DFIG parameters with a 3-phase fault in the B 34.5 kV bus, oscillation was lower during a 3 phase fault in the middle of the transmission line. It was found that the DFIG terminal voltage and 34.5 kV bus voltage were increased with the use of an ANFIS capability during a fault analysis and results are shown and oscillations observed after the transient events were damped in a very short period of time when an ANFIS was coupled to the DFIG.

VII. REFERENCES

- [1]. Pena R, Clare JC, Asher GM. Doubly fed induction generator using back-to-back PWM converters and its application to variable speed wind-energy generation. *Proc Inst Elect Eng Electr Power Appl* 1996;143(3):231-41.
- [2]. Hansen LH, Helle L, Blaabjerg F, Ritchie E, Munk-Nielsen S, Bindner H, Sørensen P, et al. Conceptual survey of generators and power electronics for wind turbines. *Risø Nat. Lab., Roskilde, Denmark, Tech. Rep. Risø-R-1205(EN)* December 2001.
- [3]. Rodríguez JM, Fernández JL, Beato D, Iturbe R, Usaola J, Ledesma P, et al. Incidence on power system dynamics of high penetration of fixed speed and doubly fed wind energy systems. Study of the Spanish case. *IEEE Trans Power Syst* 2002;17(4):1089-95.
- [4]. Meegahapola LG, Littler T, Flynn D. Decoupled-DFIG fault ride-through strategy for enhanced stability performance during grid faults. *IEEE Trans Sustain Energy* 2010;1(3):152-62.
- [5]. Hu S, Lin X, Kang Y, Zou X. An improved low-voltage ride-through control strategy of doubly fed induction generator during grid faults. *IEEE Trans Power Electron* 2011;26(12):3653-65.
- [6]. Mohseni M, Islam SM. Transient control of DFIG-based wind power plants in compliance with the Australian grid code. *IEEE Trans Power Electron* 2012;27(6):2813-24.
- [7]. Xie D, Xu Z, Yang L, Ostergaard J, Xue Y, Wong KP. A comprehensive LVRT control strategy for DFIG wind turbines with enhanced reactive power support. *IEEE Trans Power Syst* 2013;28(3):3302-10.
- [8]. Sarkhanloo S, Yazdankhah MAS, Kazemzadeh R. A new control strategy for small wind farm with capabilities of supplying required reactive power and transient stability improvement. *Renew Energy* 2012;44:32-9.
- [9]. Ling Y, Xu C. Rotor current dynamics of doubly fed induction generators during grid voltage dip and rise. *Electr Power Energy Syst* 2013;44(1):17-24.
- [10]. Ling Y, Xu C, Ningbo W. Rotor current transient analysis of DFIG-based wind turbines during symmetrical voltage faults. *Energy Convers Manage* 2013;76:910-7.
- [11]. Mohseni M, Masoum MA, Islam SM. Low and high voltage ride-through of DFIG wind turbines using hybrid current controlled converters. *Electr Power Syst Res* 2011;81(7):1456-65.
- [12]. da Costa JP, Pinheiro H, Degner T, Arnold G. Robust controller for DFIGs of grid connected wind turbines. *IEEE Trans Power Electron* 2011;58(9):4023-38.
- [13]. Kyaw MM, Ramachandramurthy VK. Fault ride through and voltage regulation for grid connected wind turbine. *Renew Energy* 2011;36:206-15.
- [14]. Yang L, Xu Z, Ostergaard J, Dong ZY, Wong KP. Advanced control strategy of DFIG wind turbines for power system fault ride through. *IEEE Trans Power Syst* 2012;27(2):713-22.
- [15]. Rahimi M, Parniani M. Grid-fault ride-through analysis and control of wind turbines with doubly fed induction generators. *Electr Power Syst Res* 2010;80(2):184-96.

- [16]. Dai J, Xu D, Wu B, Zargari NR. Unified DC-link current control for low-voltage ride-through in current-source-converter-based wind energy conversion systems. *IEEE Trans Power Electron* 2011;26(1):288-97.
- [17]. Yao J, Li H, Chen Z, Xia X, Chen X, Li Q, et al. Enhanced control of a DFIG-based wind-power generation system with series grid-side converter under unbalanced grid voltage conditions. *IEEE Trans Power Electron* 2013;28 (7):3167-81.
- [18]. Hossain MJ, Saha TK, Mithulananthan N, Pota HR. Control strategies for augmenting LVRT capability of DFIGs in interconnected power systems. *IEEE Trans Ind Electron* 2013;60(6):2510-22.
- [19]. Xiao S, Yang G, Zhou H, Geng H. An LVRT control strategy based on flux linkage tracking for DFIG-based WECS. *IEEE Trans Ind Electron* 2013;60(7):2820-32.
- [20]. Mohsen R, Parniani M. Efficient control scheme of wind turbines with doubly fed induction generators for low voltage ride-through capability enhancement. *IET Renew Power Gen* 2010;4(3):242-52.
- [21]. Mendes VF, de Sousa CV, Silva SR, Cezar Rabelo B, Hofmann W. Modeling and ride-through control of doubly fed induction generators during symmetrical voltage sags. *IEEE Trans Energy Convers* 2011;26(4):1161-71.
- [22]. Lopez J, Gubía E, Olea E, Ruiz J, Marroyo L. Ride through of wind turbines with doubly fed induction generator under symmetrical voltage dips. *IEEE Trans Ind Electron* 2009;56(10):4246-54.